Single camera spectral domain polarization-sensitive optical coherence tomography using offset B-scan modulation

Chuanmao Fan[1,2] and Gang Yao[1,3]

[1]Department of Biological Engineering, University of Missouri, Columbia, MO 65211 USA
[2]cf7b6@mail.missouri.edu
[3]gyao@missouri.edu

Abstract: We report a simple implementation to acquire spectral domain polarization-sensitive optical coherence tomography (PSOCT) using a single camera. By combining a dual-delay assembly in the reference arm and offset B-scan in the sample arm, the orthogonal vertical- and horizontal-polarized images were acquired in parallel and spatially separated by a fixed distance in the full range image space. The two orthogonal polarization images were recombined to calculate the intensity, retardance and fast-axis images. This system was easy to implement and capable of acquiring high-speed *in vivo* 3D polarization-sensitive OCT images.

© 2010 Optical Society of America

OCIS codes: (260.1440) Polarization sensitive device; (110.4500) Optical coherence tomography.

References and links

1. D. Huang, E. A. Swanson, C. P. Lin, J. S. Schuman, W. G. Stinson, W. Chang, M. R. Hee, T. Flotte, K. Gregory, C. A. Puliafito, and J. Fujimoto, "Optical coherence tomography," Science **254**(5035), 1178–1181 (1991).
2. A. F. Fercher, W. Drexler, C. K. Hitzenberger, and T. Lasser, "Optical Coherence Tomography – Principles and Applications," Rep. Prog. Phys. **66**(2), 239–303 (2003).
3. M. R. Hee, D. Huang, E. A. Swanson, and J. G. Fujimoto, "Polarization sensitive low coherence reflectometer for birefringence characterization and ranging," J. Opt. Soc. Am. B **9**(6), 903–908 (1992).
4. J. F. de Boer, T. E. Milner, M. J. C. van Gemert, and J. S. Nelson, "Two-dimensional birefringence imaging in biological tissue by polarization-sensitive optical coherence tomography," Opt. Lett. **22**(12), 934–936 (1997).
5. S. L. Jiao, and L. V. Wang, "Jones-matrix imaging of biological tissues with quadruple-channel optical coherence tomography," J. Biomed. Opt. **7**(3), 350–358 (2002).
6. B. H. Park, C. Saxer, S. M. Srinivas, J. S. Nelson, and J. F. de Boer, "In vivo burn depth determination by high-speed fiber-based polarization sensitive optical coherence tomography," J. Biomed. Opt. **6**(4), 474–479 (2001).
7. S. M. Srinivas, J. F. de Boer, H. Park, K. Keikhanzadeh, H. E. Huang, J. Zhang, W. Q. Jung, Z. Chen, and J. S. Nelson, "Determination of burn depth by polarization-sensitive optical coherence tomography," J. Biomed. Opt. **9**(1), 207–212 (2004).
8. B. Cense, T. C. Chen, B. H. Park, M. C. Pierce, J. F. de Boer, and J. F. de Boer, "Thickness and birefringence of healthy retinal nerve fiber layer tissue measured with polarization-sensitive optical coherence tomography," Invest. Ophthalmol. Vis. Sci. **45**(8), 2606–2612 (2004).
9. C. Hitzenberger, E. Goetzinger, M. Sticker, M. Pircher, and A. Fercher, "Measurement and imaging of birefringence and optic axis orientation by phase resolved polarization sensitive optical coherence tomography," Opt. Express **9**(13), 780–790 (2001).
10. E. Götzinger, M. Pircher, B. Baumann, C. Ahlers, W. Geitzenauer, U. Schmidt-Erfurth, and C. K. Hitzenberger, "Three-dimensional polarization sensitive OCT imaging and interactive display of the human retina," Opt. Express **17**(5), 4151–4165 (2009).
11. M. Zhao, and J. A. Izatt, "Single-camera sequential-scan-based polarization-sensitive SDOCT for retinal imaging," Opt. Lett. **34**(2), 205–207 (2009).
12. E. Götzinger, M. Pircher, and C. K. Hitzenberger, "High speed spectral domain polarization sensitive optical coherence tomography of the human retina," Opt. Express **13**(25), 10217–10229 (2005).
13. B. Baumann, E. Götzinger, M. Pircher, and C. K. Hitzenberger, "Single camera based spectral domain polarization sensitive optical coherence tomography," Opt. Express **15**(3), 1054–1063 (2007).
14. B. Cense, M. Mujat, T. C. Chen, B. H. Park, and J. F. de Boer, "Polarization-sensitive spectral-domain optical coherence tomography using a single line scan camera," Opt. Express **15**(5), 2421–2431 (2007).

15. C. Fan, Y. Wang, and R. K. Wang, "Spectral domain polarization sensitive optical coherence tomography achieved by single camera detection," Opt. Express **15**(13), 7950–7961 (2007).
16. B. Baumann, M. Pircher, E. Götzinger, and C. K. Hitzenberger, "Full range complex spectral domain optical coherence tomography without additional phase shifters," Opt. Express **15**(20), 13375–13387 (2007).
17. L. An, and R. K. Wang, "Use of a scanner to modulate spatial interferograms for in vivo full-range Fourier-domain optical coherence tomography," Opt. Lett. **32**(23), 3423–3425 (2007).
18. R. A. Leitgeb, R. Michaely, T. Lasser, and S. C. Sekhar, "Complex ambiguity-free Fourier domain optical coherence tomography through transverse scanning," Opt. Lett. **32**(23), 3453–3455 (2007).

1. Introduction

Optical coherence tomography (OCT) [1,2] is a powerful non-invasive optical imaging technique that can acquire high resolution depth-resolved images in highly scattering tissue specimen. Polarization-sensitive optical coherence tomography (PSOCT) [3–5] enables polarization-dependent detection in OCT and can provide additional imaging contrast such as retardance and fast-axis orientation in birefringence samples. PSOCT has been successfully applied in a variety of biomedical applications such as burn depth estimation in skin [6,7] and ophthalmology [8–10]. The recent development of PSOCT has been shifted to spectral domain implementation [11–14,11,15] due to its superior speed and sensitivity that are critical for *in vivo* three dimensional applications.

In order to extract polarization properties in a birefringence sample, at least two sample images need to be acquired with two orthogonal detection polarization states [9]. Zhao and Izatt [11] implemented a "single-camera sequential-scan-based" PSOCT system by using an electro-optic modulator to change the detection polarization between sequential scans. To further improve imaging speed, several "single-shot" PSOCT implementations have been developed. Baumann *et al* [13] used a polarization-sensitive beam splitter to direct the horizontal- and vertical-polarized components to two adjacent halves of a single spectrometer camera. Cense *et al* [14] reported a similar system where a Wollaston prism in the detection arm was used to direct the two polarization components to a single camera. Fan *et al* [15] later reported a different configuration that separated the two orthogonal polarization components in the reference arm instead of the detection arm. The two orthogonally polarized images were mapped into the two opposite sides in the full range image space relative to the zero delay line. This implementation used a common interference path in the detection arm and thus avoided the strict spatial alignment required when separating two polarization images in the detection arm. However, it required an extra phase modulation in the reference arm [15].

In this paper, we presented an improved implementation over Fan *et al*'s [15] original approach by eliminating the extra phase modulation components in the reference arm. Instead, we utilized the phase modulation provided by a galvo scanner during offset B-scans that was previously used [16–18] to achieve full range spectral domain OCT. This new implementation provided a simple solution to acquire high-speed polarization sensitive OCT images.

2. Methods

2.1 system setup

A schematic diagram of the proposed PSOCT system is shown in Fig. 1. An 844nm SLD with $\Delta\lambda$ = 46.8nm (SLD-371-HP1, Superlum, Russia) was used as the light source. The incident laser power on the sample surface was 1.3mW. The incident light was collimated and vertically polarized (V) by a polarizer after passing through an optical isolator. At the reference arm, the light was split into two parts by a non-polarized beam splitter (BS). At one arm, the vertically polarized (V) light was directly reflected by a mirror (M); while at the other arm, a quarter-wave plate (QWP) was placed at 45° to convert the back reflected light into a horizontally polarized (H) light. The H- and V-polarized reference light was recombined by the same beam splitter (BS). In the sample arm, another QWP placed at 45° converted the V-polarized incident light into circularly polarized light. The incident light was reflected at a point slightly deviated from the pivot axis at the x-y galvanometer scanner and

redirected onto an objective lens (OL). The backscattered light from the sample interfered with the horizontal- and vertical-polarized reference light separately, and were coupled into a custom designed spectrometer via a single mode fiber. The coherence spectra were captured by a line scan CCD camera with 1024 pixels (AVIIVA SM2, e2v, France) and acquired through a frame grabber (PCIe-1427, National Instruments, USA). The image acquisition speed was 50k A-line/s.
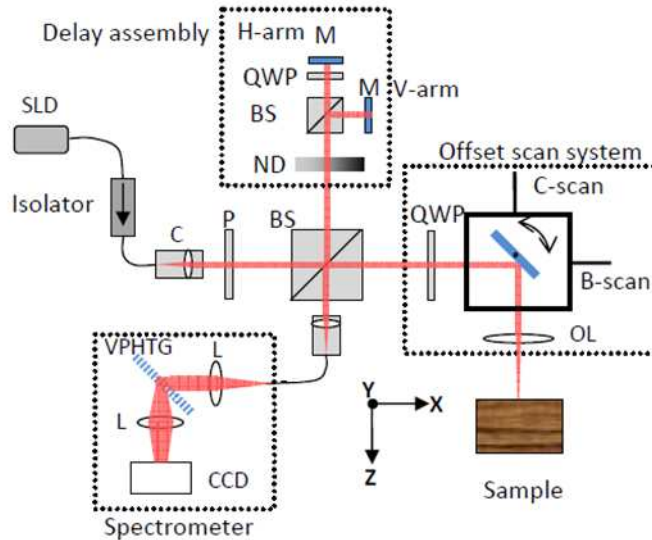

Fig. 1. A schematic diagram of the PSOCT system. SLD: superluminescent diode, C: collimator, P: polarizer to generate vertically polarized light. BS: non polarization beam splitter. ND: neutral density filter. QWP: quarter-wave plate at 45°. M: reference mirrors. L: lens. OL: objective lens (f = 88mm). VPHTG: Volume Phase Holography Transmission Grating (1200lines/mm). CCD: line scan camera.

The control signals are illustrated in Fig. 2. A digital pulse train (Ch.0) was generated from a DAQ card (PCI-6221, National Instruments, USA) to trigger the CCD line by line. This pulse train also served as the sample clock for generating saw tooth signals to control the scanner. Two voltage signals (Ch.1 and Ch.2) were used to drive the x- and y-axis galvanometer scanners to acquire the B- and C-scans, respectively.
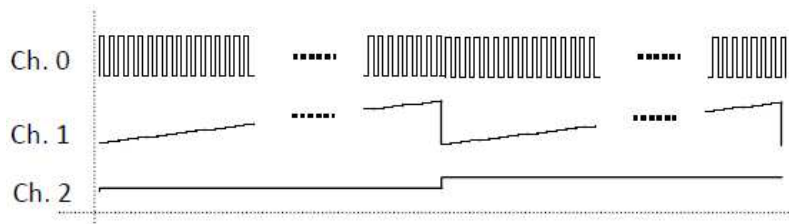

Fig. 2. Waveforms for system synchronization. Ch. 0: timing base camera trigger; Ch.1: B-scan signal; Ch.2: C-scan signal.

2.2 signal reconstruction and processing

The acquired raw OCT signal represented the summation of the H- and V-polarized interference components and can be described as:

$$I_{k,x} = I_{k,x}^0 + A_{k,x}^H \cos\left(2k(z-d) + \varphi_d\right) + A_{k,x}^V(k,x)\cos\left(2k(z+d) + \varphi_d\right), \qquad (1)$$

where $A_{k,x}^{\mathrm{H}}$ and $A_{k,x}^{\mathrm{V}}$ are the H- and V-polarized signal amplitudes at wave number k and lateral scanning position x, respectively. Similar to that in [15], the optical paths of the H and V reference were symmetrically mapped to two opposite sides ($\pm d$) of the zero delay line z = 0 (the focus plane in our configuration) by adjusting the delays in the reference arm. This configuration was necessary to shift the H and V component image adjacent to each other in the final image. The φ_d was the dynamic phase introduced by offset B-scan. φ_d was a function of the offset h related to the scanner pivot axis [16,17]:

$$\varphi_d = \frac{8\pi \cdot h \cdot \theta}{\lambda}, \tag{2}$$

where θ is the scanning angle. In order to remove the autocorrelation, self-cross correlation and fixed pattern noise, the acquired signal was preprocessed first by subtracting the average of 1000 A-scans. Then the spatial spectrum of the raw interferogram $I_{k,x}$, $B(k, f_x)$, was calculated by applying Fourier transform to the preprocessed signal against lateral position x:

$$B(k, f_x) = \frac{1}{2}(B^{\mathrm{H}}(k, f_x - f_d) + B^{\mathrm{H}}(k, f_x + f_d)) + \frac{1}{2}(B^{\mathrm{V}}(k, f_x - f_d) + B^{\mathrm{V}}(k, f_x + f_d)), \tag{3}$$

where B^{H} and B^{V} are the Fourier transform of the H and V components, respectively. The space frequency shift f_d is:

$$f_d = \frac{1}{2\pi}\frac{d\varphi_d}{dx} = \frac{4h}{\lambda}\frac{1}{\mathrm{F}}, \tag{4}$$

where F is the focal length of the imaging objective, and $x = \mathrm{F}\theta$. In the experiment, the offset and the lateral scan step size Δx were adjusted so that the spatial modulation frequency f_d was half of the maximal spatial sampling frequency $1/\Delta x$.

After obtaining Fourier transforms [Eq. (3)] on every wave number k, the resulting H- and V-polarized spectra were mirror-symmetric with zero frequency. A band-pass filter was applied to select the single side spatial spectrum. An inverse Fourier transform was then used to obtain the complex spectrum. The longitudinal (to the wave number k) Fourier transform was carried out on every calculated complex spectrum. Full range complex image was obtained with corresponding complex conjugate mirror image removed, leaving two images adjacent to each other by a distance of 2d. These two images represent these formed in horizontal and vertical polarization channels:

$$A(z, x) = A^{\mathrm{H}}(z + d, x)\exp(i\Psi_{\mathrm{H}}(z.x)) + A^{\mathrm{V}}(z - d, x)\exp(i\Psi_{\mathrm{V}}(z.x)). \tag{5}$$

To calculate polarization parameters, one image was shifted by a distance of 2d to coincide with the other. The intensity I image can be calculated as $I = \sqrt{A^{\mathrm{H}}(z, x)^2 + A^{\mathrm{V}}(z, x)^2}$. The retardance δ and fast-axis θ images were calculated using established method [3,9] as:

$$\delta = \tan^{-1}(\frac{A^{\mathrm{V}}(z, x)}{A^{\mathrm{H}}(z, x)}), \theta = \frac{\psi_{\mathrm{H}}(z, x) - \psi_{\mathrm{V}}(z, x) + \pi}{2}. \tag{6}$$

The ranges of retardation and fast axis were [0°, 90°] and [0°, 180°] respectively.

3. Results and discussion

Figure 3 demonstrated the image processing procedure described in the last section. The acquired original B-scan OCT spectra is shown in Fig. 3(a). Figure 3(b) was obtained after removing the DC components in the raw data. After Fourier transform on x, the resulting complex spectra were shown in Fig. 3(c). Both real (R) and imagery (I) parts of the result are

shown. The spectrum was modulated to be symmetric to the center zero frequency. The complex spectrum was band-pass filtered to select the single-sided spectrum. Such filtering also helped remove low frequency fixed pattern noise in the system. The Fig. 3(d) was computed by applying inverse Fourier transform to Fig. 3(c). Finally, applying Fourier transform against the wave number k produced the analytical OCT images where the H- and V-polarized components were adjacent to each other by a displacement of $2d$. After shifting one image to coincide with the other orthogonally polarized component, the intensity and retardance images can be obtained from the amplitude image in Fig. 3(e) and the fast axis image can be calculated using the phase image [Fig. 3(f)] according to Eq. (6).
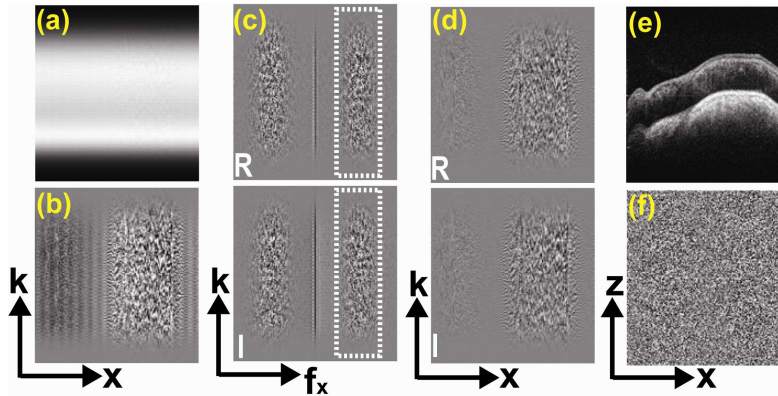

Fig. 3. An illustration of the OCT image processing. (a) The raw B-scan spectra; (b) Pre-processed spectra after removing the DC component; (c) The imaginary (I) and real (R) parts of Fourier transformed (on lateral position x) spectra. The white boxes represent the band-pass filter. (d)The complex interferogram after inverse Fourier transform of (c). The final amplitude (e) and phase (f) of the depth-resolve image were calculated by Fourier transform of (d).

During image processing, the depth-resolved signals were corrected for the sensitivity falling-off with depth whose profile approximately approached a Sinc function corresponding to Fourier transforms of the rectangular pixel sampling on the interferogram. The raw OCT signal was corrected by multiplying the inverse of the sensitivity curve. The present system had a maximum sensitivity of 104.5 dB at the zero delay line (focal plane) and minimum sensitivity of 75.5 dB at an imaging depth of 2.6 mm. The extinction ratio of complex conjugate suppression as defined in [16] was measured as 29.6 dB.
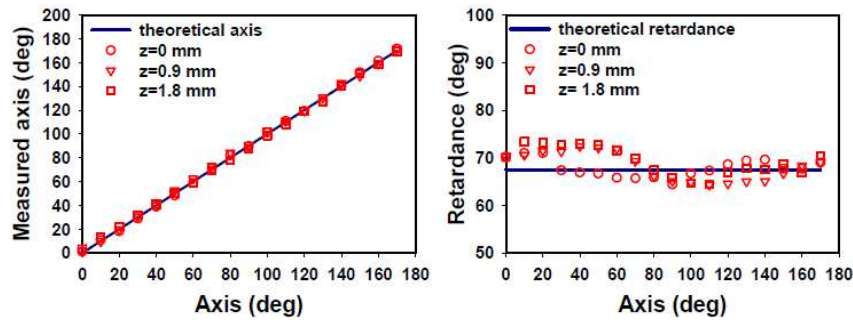

Fig. 4. The measured optical axis and retardance of a waveplate in front of a mirror. Three sets of data were measured when the mirror was placed at 0, 0.9 and 1.8mm from the focal plane.

To validate the system, a waveplate (retardance of 67.5° at 844nm) placed in front of a mirror was used as the sample. The fast axis and retardance were measured while rotating the waveplate from 0° to 170°. As shown in Fig. 4, three sets of data were measured when mirror was positioned at $z_1 = 0$ mm, $z_2 = 0.9$ mm and $z_3 = 1.8$ mm from the focal plane (zero delay

line). The measured axis orientation had good agreement with preset values with errors of [-2.5°, 1.5°], [-4.3°, 1.2°] and [-3.4°, 3.1°] at position z_1, z_2 and z_3, respectively. The corresponding measured retardance had errors between [-3.5°, 3.1°], [-4.9°, 3.2°] and [-5.9°, 3.1°]. Errors were slightly larger when the mirror was moved away from the zero delay line.

Figure 5 shows the intensity, retardance and axis orientation images obtained in a piece of chicken cartilage sample. Similar to other polarization-sensitive OCT images, the internal intensity variations suggested structural changes. The periodic changes in retardance near the sample surface revealed birefringence information of the cartilage material. The fast-axis orientation patterns coincided with the retardance changes and indicated the directional information of the organized cartilage tissue. At larger depths, the periodic changes disappeared in both retardance and fast-axis images, indicating loss of birefringence materials.
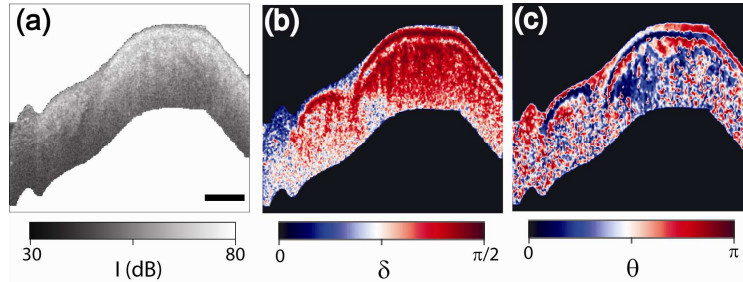

Fig. 5. the PSOCT images of a chicken cartilage sample *in vitro*. (a) Intensity; (b) retardance; and (c) fast axis orientation. The size bar indicates 500μm.

To demonstrate real time imaging, 3D *in vivo* PSOCT images were acquired from a finger fold of a human volunteer (Fig. 6). The scan contained 1000×500 A-scans at 50 kHz. The images were median-filtered. In the intensity images [Fig. 6(a)], the epidermal area could be discriminated from dermal area close to the nail fold. Cuticle, nail plate, and nail bed can be identified. The retardance image [Fig. 6(b)] revealed strong birefringence at the lower area of the nail fold. Strong birefringence was observed underneath the nail bed. Variations in dermis indicated the changes in birefringence although the same region appeared homogenous in the intensity image. Similar features were also shown in the axis image [Fig. 6(c)].
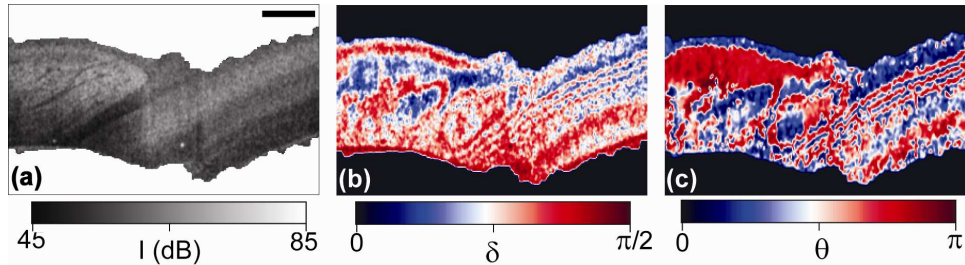

Fig. 6. 3D *in vivo* PSOCT images of a human finger fold. (a) Intensity (Media 1), (b) retardance (Media 2), and (c) fast-axis orientation (Media 3). The white size bar indicates 500 μm.

4. Summary

We implemented a full range 3D PSOCT using a single camera for parallel detection of the polarization sensitive spectral interferograms generated from H- and V-polarized components. The two orthogonal polarization channels were spatially separated by a fixed distance in the full range image space by using a dual delay assembly in the reference arm and offset B-scan in the sample arm. The separated two polarization images were recombined to obtain the retardance and axis images. By utilizing the offset B-scan method [16–18], we eliminated the additional modulation devices in a previous implementation [15]. Because a common path

was used in the detection arm for the two polarization channels, system alignment was much simplified than those required when splitting the two channels in the detection arm [13,14]. This simple system was demonstrated to be capable of acquiring *in vivo* 3D polarization-sensitive images at a speed of the 50k lines/sec, limited only by the camera speed.

Acknowledgements